Design and Analysis of a Programmable Receiver Front End Based on Baseband Analog-FIR Filtering Using an LPTV Resistor

Sameed Hameed, *Member, IEEE,* and Sudhakar Pamarti, *Member, IEEE*

Abstract—This paper presents a programmable receiver front-end that uses periodically time-varying components. A sharp programmable filtering response was achieved at RF using a linear periodically time-varying (LPTV) resistor in conjunction with a passive mixer and an integrate-and-dump circuit. The LPTV resistor along with the integrate-and-dump circuit is shown to achieve a programmable finite-impulse response (FIR) baseband filter. The baseband filter is then upconverted with the passive mixer to achieve sharp bandpass filtering at the desired RF center frequency. Further, it is shown that an additional S_{11} constraint can be imposed on the FIR filter design to allow for impedance matching to the antenna impedance. The implemented receiver achieved high close-in linearity with >17 dBm of IIP$_3$ at only 1.2× bandwidth frequency offset, while achieving a wideband impedance match with S_{11} better than −10 dB throughout the local oscillator range of 0.1–1 GHz.

Index Terms—Analog-finite-impulse response (FIR) filter, high linearity, impedance matching, linear periodically time varying (LPTV), mixer-first receiver, passive mixer, programmable receiver, sampled LPTV circuit, software-defined radio (SDR).

I. INTRODUCTION

WIDE programmability is increasingly desirable in transceiver designs. In fact, radio concepts such as cognitive radios (CRs) [1] and software-defined radios (SDRs) [2] rely on such programmability. An SDR needs to be programmable in center frequency and bandwidth (BW) to cover a large variety of frequency bands and standards at performance levels at least as good as today's conventional radios. Similarly, a CR needs to be programmable to opportunistically use temporarily unoccupied frequency bands. The primary challenge in receiver front ends is in rejecting large undesired signals (blockers) while preserving the fidelity of the desired signal. Conventional radio front ends achieve this task using sharp, off-chip SAW/BAW filters and inductor-based low-noise tuned circuits, neither of which are easily programmable. Hence, implementing wide reconfigurability in receiver front ends poses fundamental challenges.
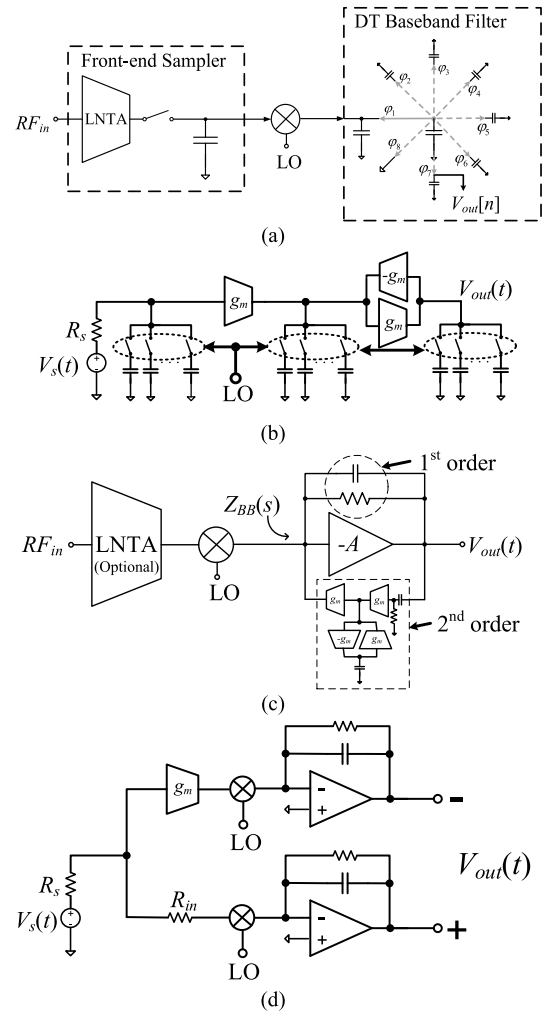
Fig. 1. Prior art in programmable receivers. (a) DT analog filters. (b) *N*-path filters. (c) Mixer-first receivers. (d) Noise cancelling mixer-first receiver.

Many approaches to reconfigurable receivers have been studied in the literature. They are all primarily based on a combination of three techniques: 1) discrete-time (DT) charge-domain signal processing [2]–[4]; 2) *N*-path filtering [4]–[8]; and 3) the mixer-first receiver topology [9]–[13], and are illustrated in Fig. 1. DT approaches rely on directly sampling the RF signal on a capacitor and subsequently processing the stored charge using switched-capacitor techniques. The

availability of high-quality switches with high sampling clock rates in deep submicrometer CMOS technologies makes this an attractive approach. One of the earliest efforts at an SDR was based on such a DT approach with multiple stages of integration sampling [2]. Subsequent works rely on implementing DT-IIR filters via charge sharing between capacitors for sharp filtering of the received signal [3], [4]. Programmability in receiver center frequency is achieved by down-conversion using DT mixers, while the BW and order of achieved filters are controlled by selecting the appropriate down-sampling rate and the number of charge sharing phases, respectively. However, DT approaches are generally limited in linearity by the first sampling stage (usually an active LNTA that is exposed to the entire RF signal swing).

Several works have used the concept of N-path filtering for implementing high-linearity receivers. By mixing the input down to dc, filtering with a simple low-pass filter, and subsequently upconverting back to RF, a high-Q bandpass filter is obtained with clock-tunable center frequency, with the BW controlled by changing the baseband filter BW. Implementing the filter with only passive components, for example, using commutating capacitors, ensures high linearity [5], [6]. Cascading such N-path filters using active stages results in an overall higher order filter, but impedance matching is a concern. For example, Darvishi et al. [7] implement a 6th-order bandpass filter in this manner. Xu et al. [4] follow N-path filtering with DT-IIR filtering to achieve higher order filters while also achieving input matching with a programmable switched-capacitor resistance. It uses only passive components for high linearity, but at the cost of noise figure (NF).

An alternative approach to apply N-path filtering is the popular mixer-first receiver topology. High linearity is achieved by eliminating the LNA and placing the antenna at the input of a passive mixer [9]. The baseband low-pass section of the mixer gets upconverted to RF to give a high-Q bandpass filter at the desired receiver center frequency set by the mixer local oscillator (LO) frequency. LO programmable matching is also possible with a resistive component in the baseband [9], but the bandpass filter is only second order with a passive first-order low-pass baseband, while NF is also high. An LNTA may instead be used for better NF, but at the cost of linearity [10]. Similarly, higher order baseband filtering [12] is possible, but linearity is degraded due to the use of active components. Murphy et al. [11] instead uses the mixer resistance to achieve a broadband match, while keeping the baseband in feedback for high linearity. As shown in Fig. 1(d), a noise cancelling current-driven path was also added for low NF, but overall linearity is high for only far-out blockers due to the first-order baseband filtering.

Hameed et al. [16] demonstrated a receiver front end with sharp programmable filtering while maintaining linearity in the presence of large close-in blockers using a new approach – one that periodically varies the value of circuit components such as resistors in time. Conceptually suggested in [14] under the moniker, filtering by aliasing (FA), and first demonstrated using a passive filter circuit [15], the technique uses a sampled linear, periodically time-varying (LPTV) circuit to realize an effective sharp linear time-invariant (LTI)
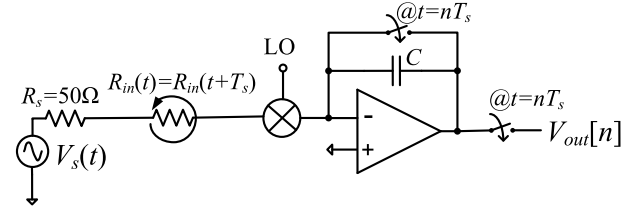

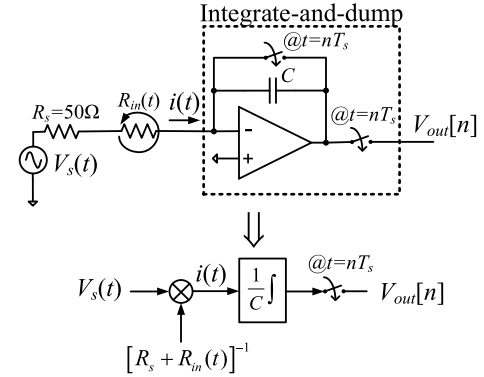Fig. 2.   Basic structure of the implemented receiver front end.

Fig. 3.   Conceptual baseband implementing analog-FIR filtering using an LPTV resistor.

filter from the input to the sampled output. While the passive filter achieves sharp programmable filtering, with high linearity and low power, it has a high NF and cannot be matched easily to the antenna interface. In contrast, Hameed et al. [16] used an active integrate-and-dump circuit in conjunction with a time-varying resistor $R_{\text{in}}(t) = R_{\text{in}}(t + T_s)$ and a passive mixer as shown in Fig. 2 to allow low noise and impedance matching as well. This paper describes the design and analysis of the LPTV receiver presented in [16] with special focus on noise and impedance matching issues.

Section II briefly reviews the LPTV filter approach and its realization in the receiver front end. Section III discusses the optimization of the filter, along with impedance matching and NF. Section IV develops the details of the circuit implementation, along with the effect of circuit nonidealities. Section V discusses the measurement results from a fabricated prototype, followed by the conclusion in Section VI.

II. RECEIVER TOPOLOGY

Consider the circuit shown in Fig. 3. While similar to the highly linear (baseband) main path of the receiver in [11] [shown in Fig. 1(d)] due to the feedback-based topology, it can be noted that the input resistance $R_{\text{in}}(t) = R_{\text{in}}(t + T_s)$ is varied periodically. Further, the baseband op-amp is configured as an integrate-and-dump circuit that resets with a period T_s that is the period of the input resistance variation. (While Fig. 3 suggests that the load capacitor needs to be instantly reset after being read, this paper uses two capacitors in a ping-pong manner so that when current is being integrated onto one, the other can be disconnected from feedback around

the op-amp, read, and then reset). Hence, the output voltage samples $V_{\text{out}}[n]$ that result from the integration of the current $i(t)$ flowing into the integrator is given by

$$V_{\text{out}}[n] = \int_{t=(n-1)T_s}^{nT_s} \frac{i(t)}{C} dt = \int_{t=(n-1)T_s}^{nT_s} \frac{V_s(t)}{C[R_s + R_{\text{in}}(t)]} dt. \tag{1}$$

If the effective filter achieved from the input $V_s(t)$ to the output samples $V_{\text{out}}[n]$ is denoted by $g(\tau)$, i.e., $V_{\text{out}}[n] = V_{\text{out}}(nT_s) = \int_{\tau=-\infty}^{\infty} g(\tau)V_s(nT_s - \tau)d\tau$, then $g(\tau)$ can simply be found from (1) to be

$$g(\tau) = \begin{cases} \dfrac{1}{C[R_s + R_{\text{in}}(-\tau)]} & 0 \le \tau < T_s \\ 0 & \text{else} \end{cases}. \tag{2}$$

Hence, it can be seen that the effective impulse response $g(\tau)$ achieved by the baseband in Fig. 3 is simply an analog finite-impulse response (FIR) filter of length T_s.

Alternatively, the realized filter response can also be derived using the concept of FA [14]. A simple block diagram of the concept is shown in Fig. 4, which consists of a simple LTI filter $h(\tau)$, whose output is sampled with a sampling period T_s. When the input to this filter is first multiplied with a periodic "spreading" signal $d(t)$ whose period is T_s, then it can be shown that the system is equivalent to the input being passed through an apparent LTI filter, $g(\tau) = h(\tau)d(-\tau)$, before sampling.

Comparing the block diagrams from Fig. 3 with the FA block diagram in Fig. 4, it can be seen on inspection that

$$d(t) = \frac{1}{R_s + R_{\text{in}}(t)}, \quad h(\tau) = \frac{1}{C}u(\tau) \tag{3}$$

where $u(.)$ is the unit-step function. Thus, the effective impulse response $g(\tau) = h(\tau)d(-\tau)$ can be verified as to be (2). Note that this interpretation might suggest that $g(\tau)$ is nonzero for all τ. However, the integrator implementing $h(\tau)$ is periodically reset, meaning that it is not strictly LTI. Hence, $g(\tau)$ is nonzero for only the duration of integration, i.e., T_s, as shown in (2).

The FIR filter described by (2) can be chosen to be any desired window function to achieve filtering. For example, setting $R_{\text{in}}(t) = R_s$ (for perfect impedance matching) realizes a rectangular window of length T_s given by

$$g_{\text{rect}}(\tau) = \frac{1}{2CR_s} \quad 0 \le \tau < T_s. \tag{4}$$

Any other desired nonnegative window of length T_s (for example, triangular, Hann, Hamming, and Kaiser [17]) can also be realized by setting $R_{\text{in}}(t)$ appropriately. Alternatively, $g(\tau)$ can be designed using any conventional digital FIR filter design technique. For this, the system can be discretized at a high oversampling rate $F_{\text{ck}} = 1/T_{\text{ck}}$, where $F_{\text{ck}}/F_s = M \gg 1$ and $F_s = 1/T_s$. Then, $R_{\text{in}}(t)$ can be replaced by its oversampled version $R_{\text{in}}[\eta] = R_{\text{in}}(\eta T_{\text{ck}})$, and so the frequency response of the discretized effective filter, $g[\eta](= g(\eta T_{\text{ck}}))$, is given by

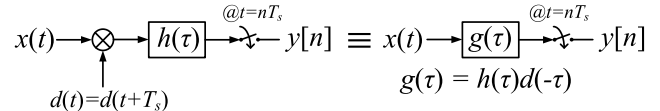$$G(e^{j\omega}) = T_{\text{ck}} \sum_{\eta=0}^{M-1} g[\eta]\exp(-j\omega\eta). \tag{5}$$

Fig. 4. Concept of FA.

The design of the filter frequency response in (5) can be treated as the design of an M-tap FIR filter design problem. Hence, any conventional DT-FIR filter design techniques such as the Parks-McClellan algorithm [18], convex optimization [19], and linear programming [20] can be used to design it as a desired low pass, high pass, bandpass, or band stop response (or a combination thereof). In this paper, the filter is designed as low-pass filters using linear programming. The optimization attempts for the highest stopband suppression (A_{stop}) for a desired passband BW F_{pass} and stopband edge F_{stop}. In practice, the resistance variation $R_{\text{in}}(t)$ can then be implemented as a sampled-and-held version of the sequence, $R_{\text{in}}[\eta]$, at the clock rate, F_{ck}, and so the continuous-time frequency response of the obtained filter is given by

$$G(f) = \frac{1}{T_s} G(e^{j2\pi f T_{\text{ck}}})\text{sinc}(f T_{\text{ck}}). \tag{6}$$

Finally, to obtain filtering at RF, an N-phase passive mixer can be incorporated into the circuit. This upconverts the baseband filter to any LO frequency as shown in Fig. 5. (Similar to the noise-cancelling mixer-first receiver [11], such a receiver operates entirely in the current domain, and so a bandpass impedance is not seen at the input.) This paper utilizes four-path mixers driven by 25% duty-cycle LO waveforms to achieve bandpass filters. Such a four-path mixer will have harmonic images of the filter passband response around odd harmonics of the LO. Nevertheless, a higher value of N can be chosen if more harmonics need to be suppressed. An example filter is shown in Fig. 5, where $F_s = 5$ MHz, $F_{\text{pass}} = 2.5$ MHz, $F_{\text{stop}} = 5$, $F_{\text{pass}} = 12.5$ MHz, and $F_{lo} = 500$ MHz. It can be noted that F_{pass} is set to $F_s/2$. This is because the FIR filter length is only $T_s = 1/F_s$ that intuitively means that the filter can only reject frequencies in the range of $1/T_s = F_s$ or higher. Increasing the filter length, T_s, simultaneously reduces the sampling rate, F_s, meaning that the passband edge, F_{pass}, will always follow the sampling frequency. This limitation can be overcome with the use of time interleaving that decouples the relationship between the FIR filter length and output sampling rate [14], [21].

III. RECEIVER FRONT-END DESIGN PARAMETERS

A. Impedance Matching

An important consideration for receiver front ends is to achieve impedance matching with the antenna impedance that is typically 50 Ω. A good match is conventionally expressed as achieving an $S_{11} < -10$ dB throughout the received channel. To achieve this, it is essential to derive the S_{11} for the proposed receiver front end. For the circuit in Fig. 5, the input impedance at any time instant, ignoring nonidealities
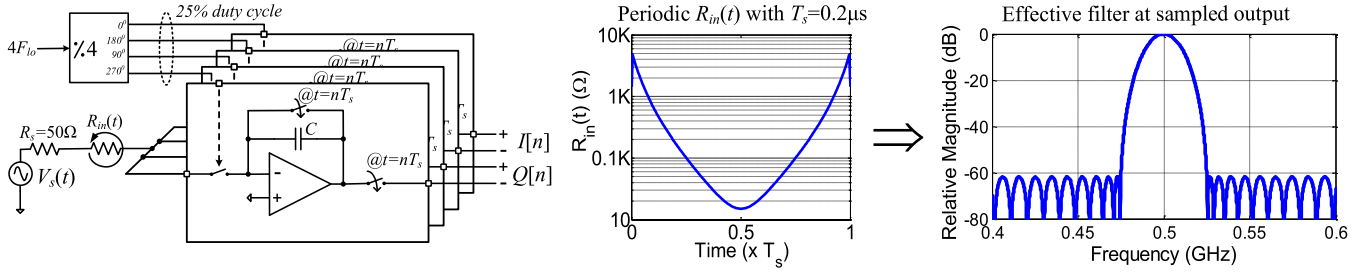
Fig. 5. Bandpass filtering by incorporating a passive mixer into the baseband filter in Fig. 3, and an example filter obtained for LO frequency of 500 MHz.

such as parasitic capacitances, is simply given by the time-varying resistance $R_{in}(t)$ (which should include the op-amp input impedance and series impedances, such as mixer switch resistance) that is a memory-less resistance. Hence, in steady state, the instantaneous ratio between the incident voltage $V_I(t)$ and reflected voltage $V_R(t)$ is given by

$$\Gamma(t) = \frac{V_R(t)}{V_I(t)} = \frac{R_{in}(t) - R_s}{R_{in}(t) + R_s}. \tag{7}$$

Note that since $R_{in}(t)$ is periodic with period T_s, $\Gamma(t)$ is also periodic with a Fourier series, $\Gamma(t) = \sum_{n=-\infty}^{\infty} \gamma_n e^{j2\pi nF_s t}$. Hence, its Fourier transform $\Gamma(f)$ is given by

$$\Gamma(f) = \sum_{n=-\infty}^{\infty} \gamma_n \delta(f - nF_s).$$

$\delta(.)$ being the Dirac delta function. To calculate S_{11} at a frequency of f_0, consider an incident voltage $V_I(t)$, consisting of a single tone at f_0, i.e., $V_I(t) = \exp(j2\pi f_0 t)$ or $V_I(f) = \delta(f - f_0)$. Then, the Fourier transform of the reflected voltage is given by

$$V_R(f) = \Gamma(f) * V_I(f) = \sum_{n=-\infty}^{\infty} \gamma_n \delta(f - f_0 - nF_s)$$

with $*$ denoting convolution. Thus, by definition, the S_{11} at frequency f_0 is simply given by the ratio between the component of the reflected and incident voltages at f_0, i.e.,

$$S_{11}(f_0) = \frac{V_R(f_0)}{V_I(f_0)} = \gamma_0 = \text{mean}[\Gamma(t)]. \tag{8}$$

Hence, the S_{11} simply depends upon the mean value of $\Gamma(t)$ given by (7). The S_{11} is frequency independent since the input impedance, while time varying, is still memory less, and so the impedance match is wideband. Nevertheless, nonidealities such as parasitic capacitances and finite op-amp BW can degrade the S_{11} at higher LO frequencies. Analyzing such effects will require the use of methods such as conversion matrices [8]. The components $\{\gamma_n\}_{n\neq 0}$ represent the fraction of incident voltage reradiated to harmonically shifted frequencies, $\{f_0 + nF_s\}_{n\neq 0}$. Such reradiation is an expected result of the LPTV nature of the circuit, and is also seen in, for example, mixer-first receivers [9].

By manipulating (8) and using (2) and (7), it can be shown that

$$S_{11} = 1 - (2R_sC)\text{mean}[g(\tau)] \quad 0 \leq \tau < T_s. \tag{9}$$

Equation (9) suggests that a good S_{11} can be achieved by adding an additional "S_{11} constraint" to the filter optimization procedure. To quantify how the achievable filter A_{stop} and S_{11} are related, the filter impulse response, $g(\tau)$, is normalized to the impedance matched rectangular window from (4). Now, (9) can be simplified to

$$S_{11} = 1 - \text{mean}[g_{norm}(\tau)] \quad 0 \leq \tau < T_s \tag{10}$$

where $g_{norm}(\tau) = g(\tau)/g_{rect}(\tau) = 2R_s/[R_s + R_{in}(-\tau)]$, with $g_{norm}(\tau) = 1$ being the trivial LTI case for perfect matching. Note that, in fact, any window function can be used to realize a perfect matched filter, $g(\tau)$, if its dc gain is scaled to give $S_{11} = 0$ according to (9), i.e., $\int_0^{T_s} g(\tau)d\tau = T_s/(2R_sC)$ or $\int_0^{T_s} g_{norm}(\tau)d\tau = T_s$. For example, a triangular window given by

$$g_{trng}(\tau) = \left[1 - \frac{|T_s - 2\tau|}{T_s}\right]\frac{1}{R_sC} \quad 0 \leq \tau < T_s$$

will give $S_{11} = 0$. Further, it can be verified that any linear combination $(1 - \lambda)g_{rect}(\tau) + \lambda g_{trng}(\tau)$, $|\lambda| \leq 1$ will still be perfectly matched.

There seems to be no obvious downside to impedance matching according to (9) and (10). However, in an actual implementation, there is a minimum value realizable for the resistance variation $R_{in}(t)$. This minimum value, R_{min}, while ideally 0, is usually set by design constraints such as area/power related to the realization of $R_{in}(t)$. For example, R_{min} is limited by the input impedance presented by the integrator, i.e., the quality of the virtual ground produced by the op-amp in Fig. 3. In addition, lower R_{min} requires larger switches in the resistor DAC (RDAC) implementing $R_{in}(t)$ as well as the mixers (leading to higher parasitic capacitances that degrade the filter response as shall be shown in Section IV). Thus, $R_{min} \leq R_{in}(t) < \infty$ leading to the additional constraint

$$0 < g_{norm}(\tau) \leq \frac{2R_s}{R_s + R_{min}}. \tag{11}$$

This condition limits the range of filters that can be attained. For example, consider the filter $(1-\lambda)g_{rect}(\tau)+\lambda g_{trng}(\tau)$. As λ increases from 0 to 1, the worst-case sidelobe suppression improves from 13 (for the rectangular window) to 26 dB (for the triangular window). But, (11) implies that $|\lambda| \leq (R_s - R_{min})/(R_s + R_{min})$. Thus, to obtain the highest sidelobe suppression, i.e., $\lambda = 1$, R_{min} must be 0. Of course, it must be noted that $R_{min} \leq R_s$ for achieving $S_{11} = 0$.
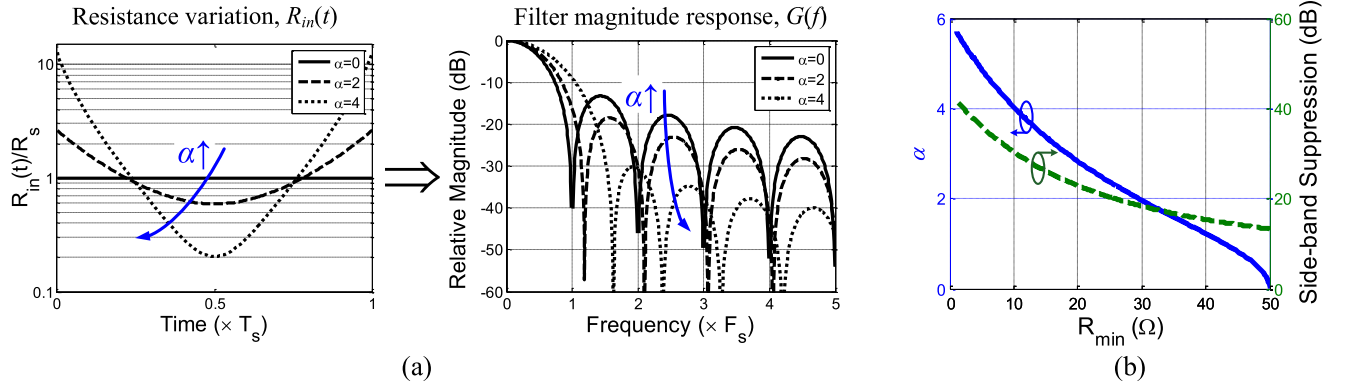
Fig. 6. (a) Change in variation of $R_{in}(t)$ on increasing parameter α, and the corresponding filter magnitude responses when $g(\tau)$ is implemented using the Kaiser window with $S_{11} = 0$. (b) Tradeoff between maximum α (and sidelobe suppression) and minimum value of $R_{in}(t)$, R_{min}, for $S_{11} = 0$ and $R_s = 50 \ \Omega$.
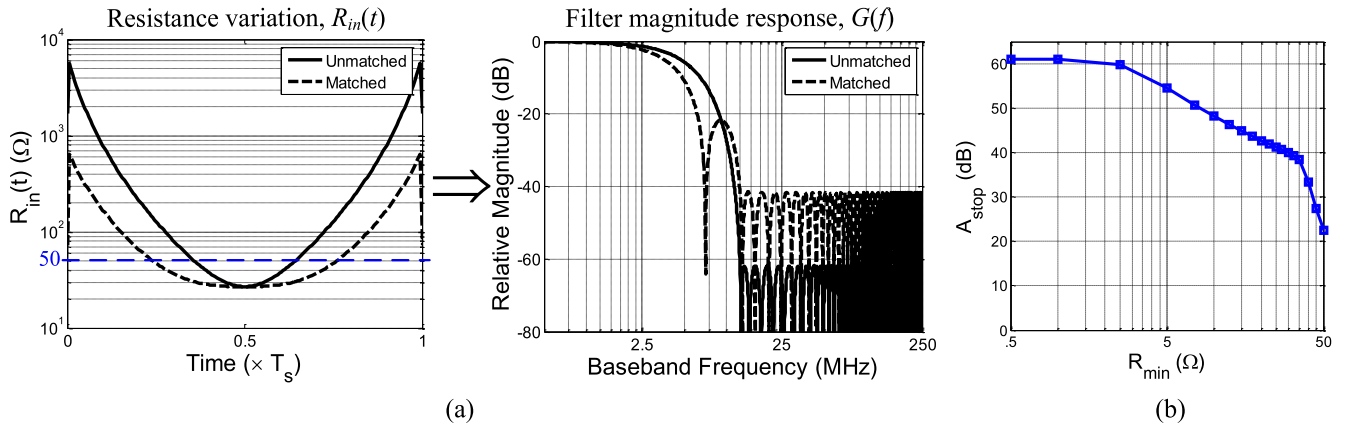

Fig. 7. (a) Example resistance variation and filter magnitude response obtained with an S_{11} requirement of -20 dB for minimum value of $R_{in}(t)$, $R_{min} = 27 \ \Omega$. (b) Achieved filter stopband suppression A_{stop} versus R_{min} for $S_{11} = -20$ dB.

Perhaps a better illustration for the limitation on sidelobe suppression is to consider the popular Kaiser window that is used to generate low-pass FIR filters. A Kaiser window [17] of length T_s is given by

$$g_{kaiser}(\tau) = \frac{I_0[\alpha\sqrt{1 - \{(\tau - 0.5T_s)/0.5T_s\}^2}]}{I_0[\alpha]} \quad 0 \le \tau < T_s$$

where $I_0(.)$ is the zeroth-order modified Bessel function of the first kind, and α is used to vary the window sidelobe suppression (higher α for more suppression [17]). As shown in Fig. 6(a), as α increases the range of variation of $R_{in}(t)$ also increases, meaning that R_{min} must be reduced to obtain $S_{11} = 0$. Hence, a limited R_{min} implies a maximum value for α, and thus limited sidelobe suppression. Fig. 6(b) shows the maximum α and sidelobe suppression versus R_{min}, and shows the clear tradeoff between R_{min} and the filter suppression achieved with impedance matching. Thus, it can be expected that impedance matching will result in lower stopband suppression.

In the general filter design problem, an additional constraint $|S_{11}| \le \beta$ can be added using (10), where β is the desired S_{11}, while satisfying (11). These two constraints can be combined to give the constraint

$$\left| 1 - \frac{2R_s}{R_s + R_{min}} \text{mean}[g_{norm}^{max}(\tau)] \right| \le \beta \quad 0 \le \tau < T_s \quad (12)$$

where

$$g_{norm}^{max}(\tau) = \frac{g(\tau)}{g_{max}} = \frac{R_s + R_{min}}{R_s + R_{in}(-\tau)}$$

and g_{max} is the peak value achievable by $g(\tau)$, i.e., $g_{max} = 1/[C(R_s + R_{min})]$. The S_{11} constraint given by (12) essentially restricts the range of variation of the impulse response, or equivalently the resistance variation, $R_{in}(t)$. For example, Fig. 7(a) shows the resistance variation obtained with and without the additional constraints for S_{11} of -20 dB for $R_s = 50 \ \Omega$, and $R_{min} = 27 \ \Omega$ (similar to the implementation in this paper). The matched case clearly has lower resistance variation, and hence, sacrifices A_{stop} to achieve the desired S_{11}. The variation of A_{stop} achieved while varying R_{min} is also shown in Fig. 7(b). It can be seen that R_{min} needs to reduce to $\sim 1\Omega$ to obtain the same A_{stop} as the unmatched case.

Fig. 8 shows the variation A_{stop} achieved with required S_{11} for various transition BWs of $K = F_{stop}/F_{pass}$, with $F_{pass} = F_s/2$, $R_s = 50 \ \Omega$, and $R_{min} = 27 \ \Omega$ (similar to the
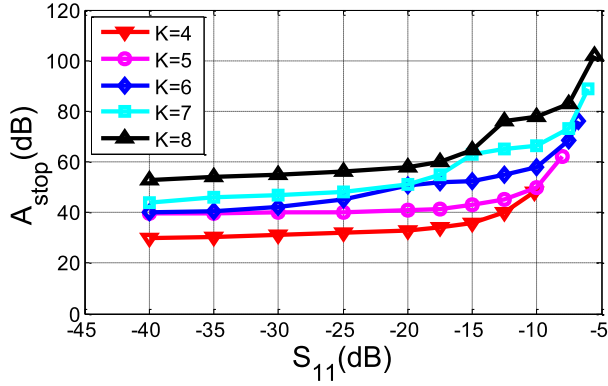
Fig. 8. Achieved filter stopband suppression A_{stop} versus S_{11} required, where $K = F_{stop}/F_{pass}$ with F_{pass} and F_{stop} being the filter passband and stopband edges, respectively.

implementation in this paper). While A_{stop} does improve with increasing transition BWs, it can be seen that the improvement is far less compared to the unmatched case (corresponding to the point with worst S_{11} in each curve).

B. Noise Figure

The addition of time-varying components such as LPTV resistors significantly improves the filtering performance of the receiver front end. However, analyzing the noise performance of such a receiver is not trivial. In the conventional mixer-first receiver, the baseband filter is LTI, and so its noise analysis is straightforward. However, in the implemented front end, the inherent LPTV nature of the baseband filter and the aliasing involved in the inherent sampling operation must be accounted for.

1) Noise Factor: The noise performance of the circuit is analyzed in Appendix A. It is shown that for an op-amp implemented as a simple g_m stage, the noise factor F of the circuit, compared to the contribution of the source R_s, is given by (24) as

$$F = 1 + \frac{\gamma}{g_m R_s} + \frac{\text{mean}\left[\left(R_{in}(t) - g_m^{-1}\right)/(R_s + R_{in}(t))^2\right]}{R_s \text{mean}[1/(R_s + R_{in}(t))^2]}. \tag{13}$$

This expression can be further simplified for $\gamma = 1$ (short channel-length devices) to give

$$F = \frac{\text{mean}[1/(R_s + R_{in}(t))]}{R_s \text{mean}[1/(R_s + R_{in}(t))^2]}$$
$$= \frac{\text{mean}[g_{norm}(\tau)]}{\text{mean}[g_{norm}^2(\tau)]} \quad 0 \le \tau < T_s. \tag{14}$$

It can be easily seen that for $R_{in}(t) = R_s$ [or $g_{norm}(\tau) = 1$], i.e., the LTI case, $F = 1 = 3$ dB as expected.

2) Aliasing: Appendix B describes the NF contribution from aliasing. Using (27), it can be shown that the noise factor degradation due to aliasing at dc, i.e., the baseband frequency, $\Delta f = 0$ is given by

$$F_{aliasing}(\Delta f = 0) = \frac{\text{mean}[(R_s + R_{in}(t))^{-2}]}{\{\text{mean}[(R_s + R_{in}(t))^{-1}]\}^2}$$
$$= \frac{\text{mean}[g_{norm}^2(\tau)]}{\text{mean}[g_{norm}(\tau)]} \quad 0 \le \tau < T_s. \tag{15}$$
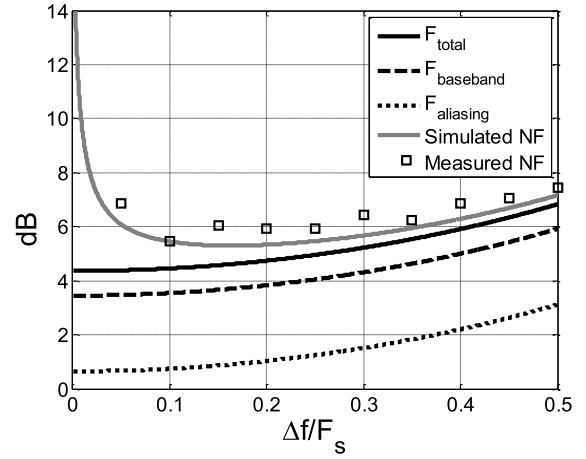

Fig. 9. Calculated NF for the impedance matched filter shown in Fig. 7(a), and comparison with the simulation and measured results.

So, using (15) and (28), the total baseband noise factor at baseband frequency Δf is given by

$$F_{baseband}(\Delta f)$$
$$= F \times F_{aliasing}(\Delta f)$$
$$= \left|\frac{G(\Delta f = 0)}{G(\Delta f)}\right|^2 \frac{2}{\text{mean}[g_{norm}(\tau)]} \quad 0 \le \tau < T_s. \tag{16}$$

Interestingly, $F_{baseband}(\Delta f = 0) = 2/(1 - S_{11})$, i.e., the baseband noise factor at dc is related to the achieved S_{11}. Further, in the case of perfect matching $S_{11} = 0$, and so $F_{baseband} = 2$ at dc that is the same as the LTI case, i.e., there is no degradation due to the time-varying resistance. The additional degradation at other frequencies is due to droop in the filter response. In an LTI front end, there is usually no additional degradation since the out-of-band noise is usually filtered-off by downstream stages.

3) Harmonics: It must be noted that when operated as a bandpass filter with an N-path passive mixer, the NF degradation due to LO harmonics has to be added as well as is given by [11]

$$F_{harmonics} = \frac{1}{\text{sinc}^2(1/N)}. \tag{17}$$

For a four-path mixer, $F_{harmonics} \approx 0.91$ dB. Alternatively, the harmonic contribution can also be included as part of aliasing, with the filter frequency response replaced by the bandpass frequency response (that includes harmonic images caused by the four-path mixer).

Thus, the total NF is given by

$$F_{total}(\Delta f)|_{dB} = 10 \log_{10}[F \times F_{aliasing}(\Delta f) \times F_{harmonics}]$$
$$= F|_{dB} + F_{aliasing}(\Delta f)|_{dB} + F_{harmonics}|_{dB}. \tag{18}$$

where $F_{harmonics}$ only appears with bandpass operation. Fig. 9 shows the calculated NF of the impedance-matched filter shown in Fig. 7(a) along with the simulation and measured results for the same filter with $F_s = 5$ MHz and $F_{lo} = 500$ MHz. It can be seen that the calculated $F|_{dB} = 2.75$ dB, $F_{aliasing}(\Delta f = 0)|_{dB} = 0.72$ dB, and the average NF across

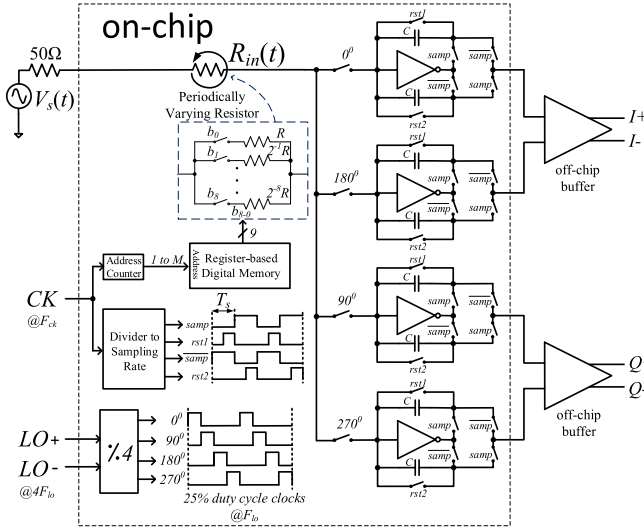Fig. 10.   Block diagram of the implemented receiver front end.

Fig. 11.   Schematic of the 9-bit RDAC with annotated switch parasitics.

frequencies is 5.2 dB. (The filter droop across the band is about 2.2 dB.) It can also be simply noted that $F|_{\text{dB}} + F_{\text{aliasing}}$ $(\Delta f = 0)|_{\text{dB}}$ is very close to the 3 dB obtained in case of LTI operation (due to $S_{11} = -20$ dB $= 0.1$). The simulation and measured results closely match the calculations. The constant degradation of ~ 0.3 dB seen compared to calculations is due to loss from the parasitic capacitance at the RDAC input (from the package, pad, and RDAC switches), while the degradation at low offset frequencies is due to flicker noise from the op-amps, and has a corner frequency of ~ 100 kHz. As expected, the NF increases at higher Δf due to filter droop. While this is unavoidable, the noise degradation can be reduced by setting the sampling rate F_s, such that the received signal single-sideband BW is lower than, for example, $0.25 F_s$, thus ensuring that $F_{\text{baseband}}(\Delta f)|_{\text{dB}} < 4$ dB inside the signal band (as observed from Fig. 9). This does come at the cost of not filtering the adjacent band to the wanted signal.

IV. IMPLEMENTATION AND NONIDEALITIES

The block diagram of the implemented FA-based receiver front end is shown in Fig. 10. The antenna input is connected to the LPTV resistor $R_{\text{in}}(t)$ that is built as a 9-bit RDAC. The RDAC control bits are periodic with the period T_s and are read out periodically from an on-chip register-based memory at the input clock rate $F_{\text{ck}}(= MF_s)$, $M \gg 1$. The RF current is mixed down to baseband with a four-path 25% duty-cycle mixer switching at the LO frequency, F_{lo}. The mixer switches use transmission gates and have a resistance of about 3 Ω. The baseband is composed of integrators with self-biased inverter-based op-amps whose sampling and reset clocks are generated by dividing F_{ck}.

A. Resistor DAC

The heart of the receiver front end is the 9-bit RDAC shown in Fig. 11. As shown, the RDAC is implemented in a binary-scaled fashion, with each branch consisting of several
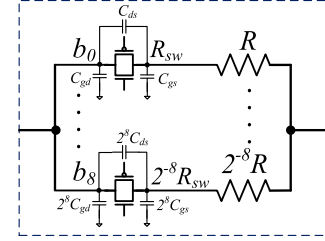
unit resistor cells connected in parallel. Each cell consists of an *rppoly* resistor of value R in series with a transmission gate control switch with resistance R_{sw}. The minimum RDAC resistance was designed to be about 15.7 Ω ($2^9 - 1$ unit cells is parallel, each with resistance $R + R_{\text{sw}} \approx 8$ kΩ). The output node of the RDAC is held at virtual ground due to the op-amp, and so the input swing is divided across the linear poly resistor and the nonlinear control switch. Hence, to maximize the out-of-band linearity of the circuit (when the op-amp outputs do not compress), the ratio of switch resistance R_{sw} to the poly resistance R must be minimized. However, lower R_{sw} implies larger switches, and hence higher power consumption for driving them. Furthermore, the parasitic capacitances associated with switch transistors shown in Fig. 11 increase with size as well, and hence, limit the filtering performance as well. To balance these effects, $R_{\text{sw}} : R$ was set to 1:4.

A consequence of implementing the LPTV as an RDAC with switched controls is that the resistance variation $R_{\text{in}}(t)$ is implemented as a sampled-and-held waveform (instead of a fully continuous-time waveform). The filter response obtained with such a switched implementation leads to the images of the filter passband appear every F_{ck}, but filtered by the nulls of the sinc [as shown in (6)] due to sample-and-hold operation. An example can be seen in Fig. 12(a) for the case of a low $M = 20$. The worst-case image power is around $f = F_{\text{ck}} - F_{\text{pass}}$, with a suppression of about $(1 - \delta_{\text{pass}})\text{sinc}(1 - F_{\text{pass}}T_{\text{ck}})$, where F_{pass} is the passband BW, and δ_{pass} is the passband ripple. For typical values of $1 - \delta_{\text{pass}} \approx -3$ dB (assuming filter BW is represented by -3 dB BW), and $F_{\text{pass}} = F_s/2$, the image suppression is plotted versus oversampling rate in Fig. 12(b). F_{ck} should hence be chosen such that the suppression $\approx A_{\text{stop}}$. For A_{stop} of 50 dB, an oversampling factor of 100 is sufficient.

Another important factor that determines the actual filter shape and A_{stop} achieved is the precision of the resistance variation $R_{\text{in}}(t)$. Due to the RDAC implementation, $R_{\text{in}}(t)$ is quantized. Fig. 13 shows the effects of quantization on the filter magnitude response, when $R_{\text{in}}(t)$ is implemented as a binary-scaled RDAC with a minimum resistance of 16 Ω and an additional 11 Ω of constant series resistance added due to op-amp input impedance and mixer switch resistance (similar to this paper). It can be noted that about 8 bits of accuracy are required to guarantee higher than 50 dB of A_{stop}.

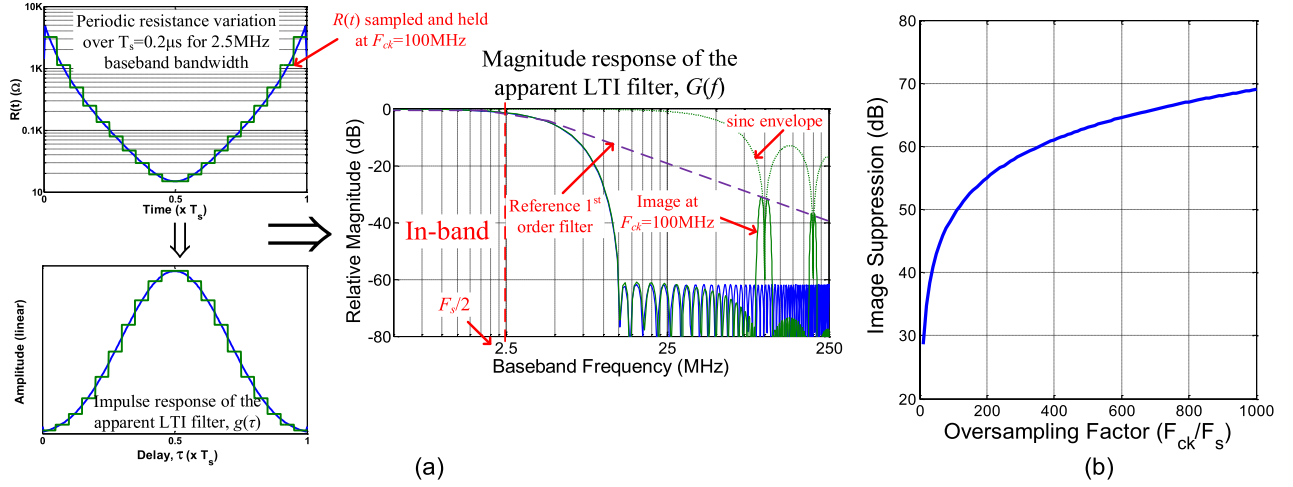The effect of the switch parasitics is considered below, and is similar to the passive LPTV scanner described in [15].

Fig. 12. (a) Example resistance variation $R_{\rm in}(t)$, and the corresponding impulse response $g(\tau)$ and magnitude response $G(f)$ shown for the case of: 1) blue: oversampling factor, $M = F_{\rm ck}/F_s \to \infty$ and 2) green: $M = 20$. (b) Variation of image suppression with M.
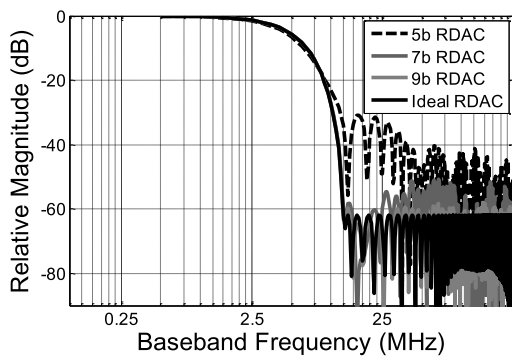

Fig. 13. Achieved filter magnitude response versus accuracy of resistance variation $R_{\rm in}(t)$.
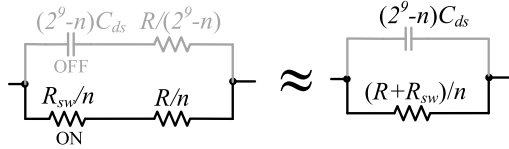

Fig. 14. Effect of parasitic $C_{\rm ds}$ capacitance on the RDAC.

1) C_{ds} Capacitance: $C_{\rm ds}$ is mainly present due to routing and so can be minimized to some level during layout. Fig. 14 shows the effective circuit of the RDAC when set to a code of n with $C_{\rm ds}$ considered. The switches in the ON branches simply present an effective resistance of $R_{\rm sw}/n$ as shown, while those in the OFF branches instead produce an effective capacitance of $(2^9 - n)C_{\rm ds}$. Since the corner frequency $1/2\pi RC_{\rm ds} \gg F_{\rm ck}$, the RDAC is effectively a resistance in parallel with a capacitance, with a code-dependent corner frequency. Moreover, the corner worsens for small n limiting RDAC dynamic range, and thus, limits the filter suppression achieved. Fig. 15 shows the simulated effect of $C_{\rm ds}$ on a 5-MHz-BW filter centered at 500 MHz and compares it to the measured results. It is clear that the $C_{\rm ds}$ limits the filter
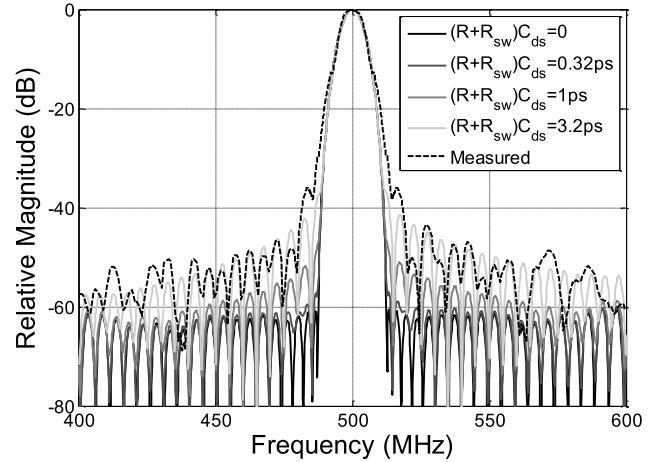

Fig. 15. Simulated effect of parasitic $C_{\rm ds}$ capacitance on filter magnitude response.

attenuation in this paper due to the value of $(R + R_{\rm sw})C_{\rm ds} \approx$ 3.2ps. This issue can be remedied with the additional of cross-coupling capacitors. An example of this technique was shown in [21] for a differential implementation.

2) C_{gs}/C_{gd} Capacitance: The $C_{\rm gs}$ and $C_{\rm gd}$ capacitances are mainly due to the switch transistors themselves. $C_{\rm gd}$ presents itself directly at the antenna and reduces gain (and worsens NF) at high LO frequencies, while degrading the S_{11} as well. $C_{\rm gs}$ capacitances in the RDAC draw current from the source in a code-dependent manner. The simulated effects of both $C_{\rm gs}$ and $C_{\rm gd}$ on a 5-MHz-BW filter centered at 500 MHz is shown in Fig. 16 with $C_{\rm gd} = C_{\rm gs}$. As can be seen, only the filter transition band is affected, and the effect is small compared to that of $C_{\rm ds}$ (unlike for the passive filter [15]). In this paper, $R_{\rm sw}C_{\rm gs} \approx 3.2$ps. Note that $R_{\rm sw}C_{\rm gs}$ will scale with process.

B. Baseband Integrators

The baseband integrators consist of simple inverter-based op-amps with tunable capacitor banks in feedback around
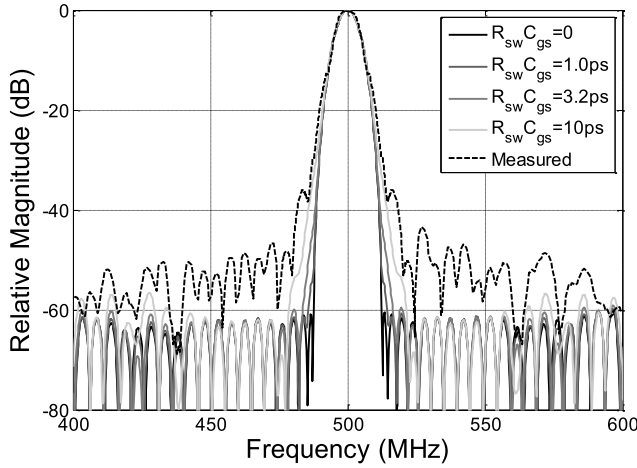
Fig. 16.   Simulated effect of parasitic C_{gs}/C_{gd} capacitance on filter magnitude response.
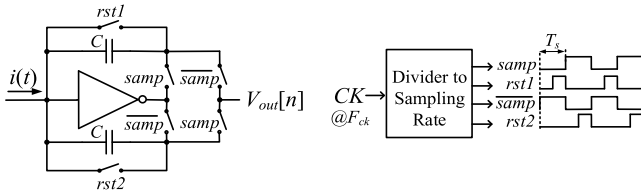

Fig. 17.   Inverter-based baseband integrator schematic and clocks.

them, as shown in Fig. 17. Each capacitor bank is built as a ping-pong structure. This allows one capacitor to be connected across the op-amp, while the voltage stored on the other can read and reset using the clocks shown. For example, when samp = 1, the upper capacitor is connected in feedback around the op-amp while the lower capacitor is connected to the output, read, and then reset using the signal, rst2 (and vice versa when samp = 0, with reset controlled by rst1 instead). The capacitor banks use MIM capacitors and are tunable from 20–140 pF to allow for a wide range of filter BWs, and their parasitics have no noticeable effect on performance. The op-amps themselves are self-biased due to the ping-pong action. Each op-amp consists of a PMOS and NMOS of length 180 nm to increase gain to about 20 dB and to reduce the flicker noise corner, and has a transconductance, g_m, of 125 mS. The g_m is chosen to minimize NF contribution, as well as to minimize the minimum resistance achievable at the front end, R_{min}, to aid in impedance matching.

The effects of op-amp nonidealities such as finite gain and BW are considered in the equivalent circuit shown in Fig. 18. The op-amp is single stage with gain A, transimpedance g_m, and output impedance R_o. The block diagram for the circuit operation (obtained from its differential equation) is also shown. While the filter impulse response can be derived from the block diagram, finite gain and BW are considered separately for simplicity, especially since the former only affects low-frequency operation, while the latter affects only high frequencies.

1) Finite Op-Amp Gain: Consider the case where the op-amp has an open-loop gain of A, while its BW is unlimited ($g_m \rightarrow \infty$). The equivalent circuit can be easily understood as a time-varying passive RC circuit formed by the input resistance and a capacitance $(1 + A)C$ produced by the Miller effect. Hence, the block diagram (and filter impulse response) can be derived by simply modifying the one for the passive filter in [15]. The block diagram obtained (shown in Fig. 18), reveals that the difference compared to the fully passive case is that the feedback path (corresponding to integrator leakage) is attenuated by the op-amp gain. The simulated effect of op-amp gain is plotted in Fig. 19 for a 5-MHz-BW filter centered at 500 MHz, with $C = 100$ pF along with the calculated results that match quite precisely. The ideal gain of a single path in the four-path bandpass circuit is about 10 dB. Hence, the filter gain and shape degrade when op-amp gain reaches close to the ideal path gain. Nevertheless, the effect is small, and can be alleviated by increasing C to reduce filter gain (similar to other switched-capacitor circuits).

2) Finite Op-Amp Bandwidth: If the transconductance g_m is finite (while $A \rightarrow \infty$), the integrator BW is only $BW_{int} = g_m/C$. In this configuration, the input impedance of the op-amp is given by $1/g_m$ and has to be included with the input resistance seen by the source. Further, at high frequencies, the op-amp is diode-connected and so the output voltage simply reduces to a voltage division $g_m^{-1}/(R_s + R_{in}(t) + g_m^{-1})$. Thus, the equivalent block diagram reduces to the one shown in Fig. 18, where the integrator input current is determined by the total resistance, $R_s + R_{in}(t) + g_m^{-1}$, while the high-frequency voltage division produces an input-to-output leakage path. Since the leakage path has no memory and the output is sampled, its value matters only at the sampling instant. Thus, it acts as an all pass filter with gain $\sim 1/g_m R_{in}(T_s)$, compared to the desired filter gain set by $1/C$. If the relative level between the gains, i.e., $g_m R_{in}(T_s)/C = BW_{int} \times R_{in}(T_s)$ is lower than A_{stop} of the desired filter, then the all-pass filter dominates in the stopband. Thus, the stopband suppression of the filter is degraded if BW_{int} is low enough. The simulated effect of op-amp g_m is plotted in Fig. 20 for a 5-MHz-BW filter centered at 500 MHz, with $C = 100$ pF along with the corresponding calculated results. It can be seen that the filter suppression is set by the leakage path as g_m reduces. Nevertheless, the leakage depends on $R_{in}(T_s)$ as well. Hence, if the filter design problem is tweaked such that $R_{in}(T_s) \rightarrow \infty$, i.e., the filter is designed for $M - 2$ taps with $g[0] = g[M - 1] = 0$ in (5), then the effect of the leakage path should be remedied. This should eliminate the effect of finite g_m on stopband suppression.

The effects of finite op-amp gain and BW described above can now be combined to approximate the actual impulse response of the filter (instead of deriving it from the combined model in Fig. 18, though it is more precise). This simply means including $1/g_m$ in the input impedance while computing the impulse response using the finite gain model, and then in addition including the input-to-output leakage term. Fig. 21 shows the simulation and calculated effect of finite op-amp gain and g_m for a 5-MHz-BW filter centered at 500 MHz, with $C = 100$ pF. Improving the response is accomplished
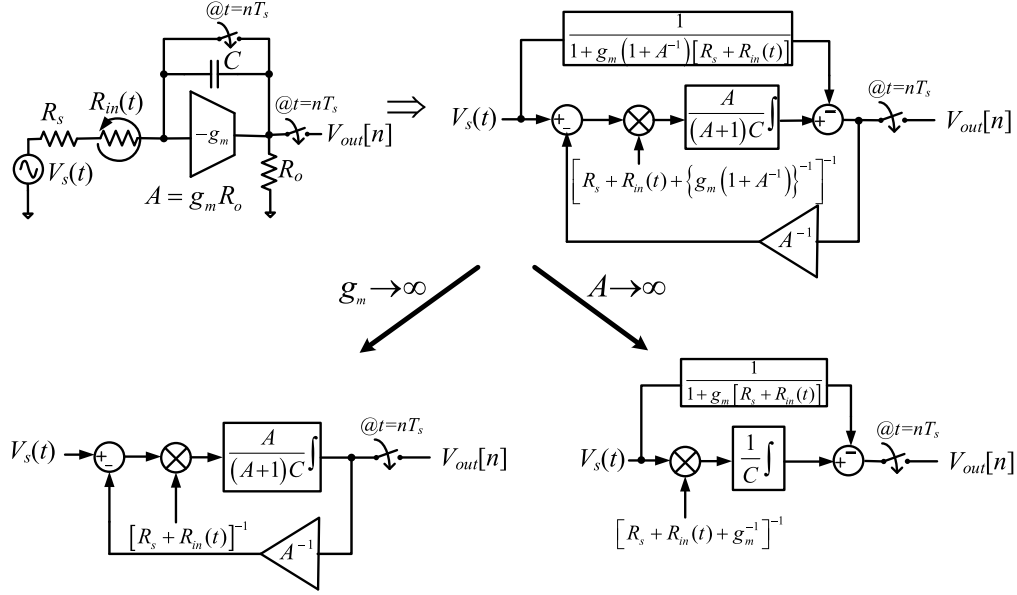
Fig. 18. Equivalent circuit and block diagram for finite op-amp gain A and BW g_m/C, and simplified models for either finite gain or finite BW.
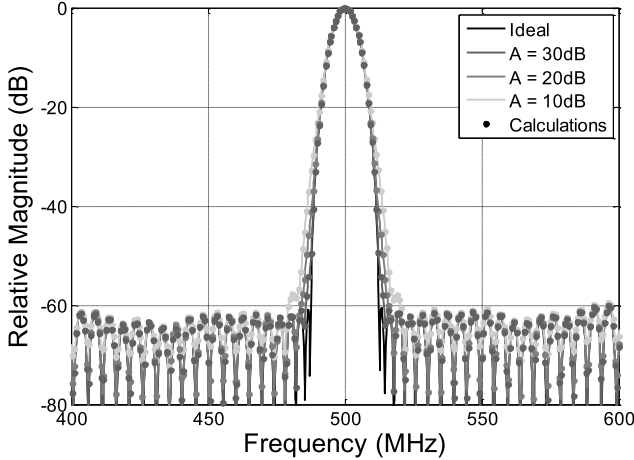

Fig. 19. Simulated effect of finite op-amp gain A on filter magnitude response, and comparison with calculations.
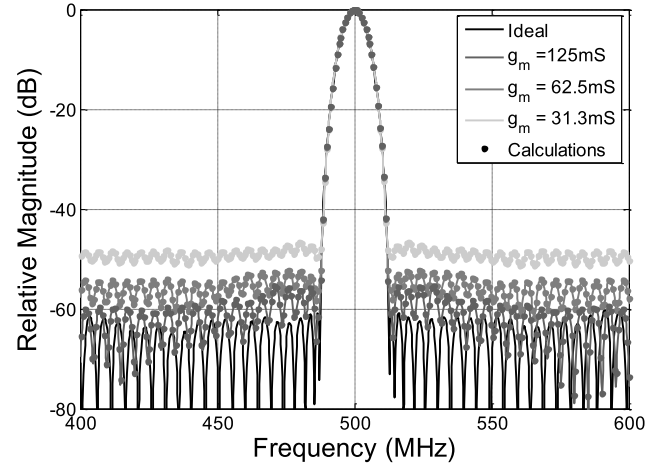

Fig. 20. Simulated effect of finite op-amp g_m on filter magnitude response, and comparison with calculations.

by setting $R_{\rm in}(T_s) \rightarrow \infty$ (as explained previously). Now, the filter response matches the case of finite gain only, i.e., the degradation of the filter stopband due to finite op-amp g_m is alleviated.

V. MEASUREMENT RESULTS

The receiver front-end IC was fabricated in TSMC 1P6M 65-nm CMOS process and was packaged in a 40-pin 5 mm × 5 mm QFN package. Fig. 22 shows the micrograph of the implemented IC. It has an active area of 2 mm^2, about 2/3 of which is occupied by capacitors. Note that capacitor area can be significantly reduced while operating with higher filter BWs.

A supply voltage of 1.2 V is used for the op-amps, the LO dividers, as well as the drivers for controlling the RDAC

and LO switches. The dc bias of the entire chain is set to around 0.6 V due to the op-amp biasing at reset. The rest of the (mostly digital) circuitry runs on a 1-V supply. For a 5-MHz RF BW filter centered at $F_{lo} = 500$ MHz, the 1.2-V supply draws a current of 57 mA from the supply, with each op-amp consuming 13 mA, the LO divider and switch drivers consuming about 5 mA. The digital and clock generation blocks draw 2 mA from the 1-V supply for a nominal clock frequency of $F_{\rm ck} = 1$ GHz. The system was verified to work up to $F_{\rm ck} = 2$ GHz for use with higher filter BWs.

The sampled-and-held IC outputs are buffered externally for measurements. Four filter configurations were considered– filters 1, 2, and 3 were designed with an S_{11} constraint of -20 dB and different transition BWs, while filter 4 only had a transition BW constraint. Fig. 23(a) shows the measured
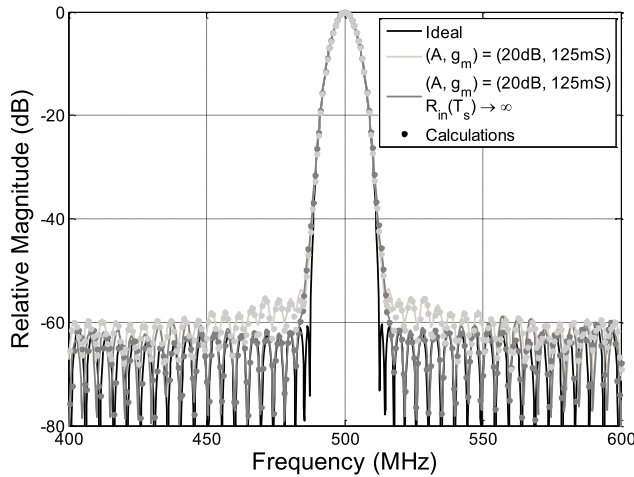
Fig. 21.   Comparison of simulations and calculations for combined effect of finite op-amp gain (A) and BW (g_m) on filter magnitude response.
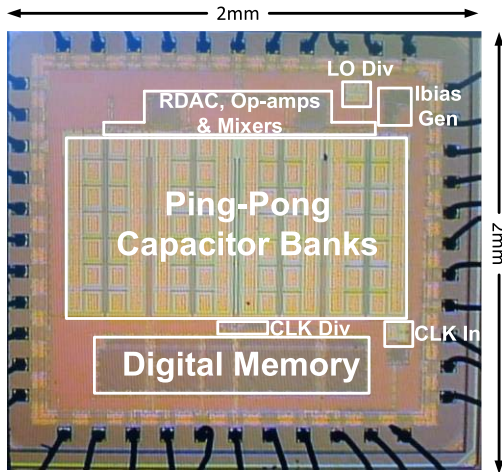

Fig. 22.   Chip micrograph.

Fig. 23.   (a) Measured 5-MHz RF BW (2.5-MHz baseband BW) filter responses. Filters 1–3 are designed with an S_{11} constraint of −20 dB. (b) Filter 1 responses for RF BW tuned from 2.5–40 MHz. (c) Filter 4 responses for the LO varied from 0.1 to 1 GHz.

frequency response of the filter in these configurations (plotted along with the first- and second-order Butterworth filter responses for comparison). The receiver gain obtained for the 5-MHz RF BW (2.5-MHz baseband BW) filter with $C = 100$ pF was 18.9 dB when configured for matching (filters 1, 2, and 3) and 15.4 dB for filter 4. The transition BWs for filters 1, 2, 3, and 4 were 12.5, 22.5, 32.5, and 17.5 MHz, respectively, while the achieved stopband rejection was observed to be better than 35, 45, 50, and 48 dB, respectively. The large sidelobes in filters 1–3 are simply because no constraints were placed on the transition band in the FIR filter optimization [for example, the filter response in Fig. 7(a)]. While such constraints can be added, it will result in degraded stopband rejection. The filter RF BW was varied from 2.5 to 40 MHz [Fig. 23(b)] by varying the resistor variation period (and sampling interval) T_s. The gain scales linearly with T_s and inversely with C. F_{lo} were also varied from 100 MHz to 1 GHz, as shown in Fig. 23(c). The gain reduced by ~ 2 dB from $F_{lo} = 100$ MHz to 1 GHz.
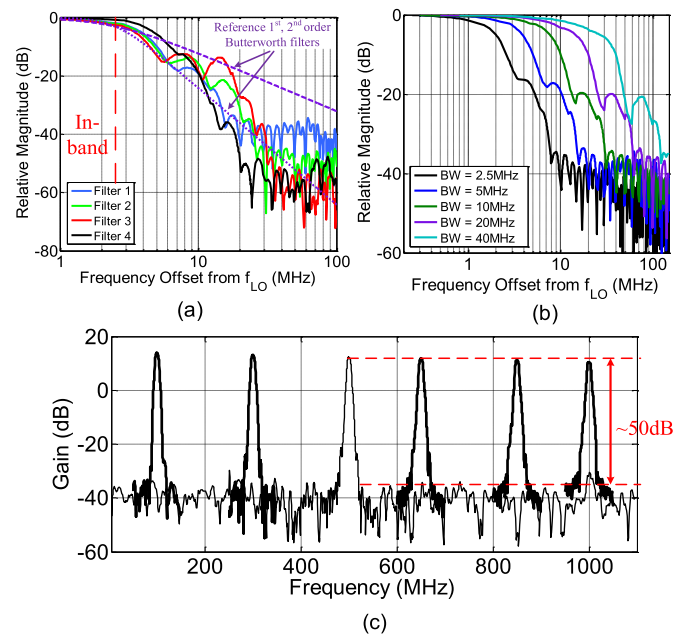
Fig. 24 shows linearity measurements. The two input tones are chosen such that the intermodulation products are generated at an offset frequency of 0.5 MHz. For a 5-MHz-BW filter 1 configuration (designed for matching) with $F_{lo} = 500$ MHz and $C = 100$ pF, while the in-band IIP$_3$ was measured to be about +1 dBm, OOB IIP$_3$ was better than +17 dBm, and OOB IIP$_2$ was better than +60 dBm without calibration, both at 6-MHz offset from the carrier. The OOB IIP$_3$ is limited by the nonlinearity due to the RDAC (and mixer) switches, while the in-band IIP$_3$ is dominated by the compression at the op-amp output. Fig. 25 shows S_{11} and blocker NF measurements. The S_{11} was better than −11 dB for the entire receiver LO range. Note that the S_{11} worsens at higher LO frequencies due to the presence of parasitic capacitances from the RDAC, as well as the pads, package, and the PCB. The measured NF was 6.5 dB. The NF degraded by 12 dB if a 0 dBm blocker was present at 16-MHz offset. The degradation is mostly caused due to the nonoptimized design of the LO divider and not due to circuit nonlinearity. (Simulated LO divider phase noise at blocker offset was −155 dBc/Hz.) Further, the issue does not arise in [21] with an improved LO divider design. The measured blocker NF does not vary significantly with blocker offset frequency due to the high divider phase noise. It should be noted that if matching is not needed (filter 4 configuration), the in-band IIP$_3$ improves to +5 dBm, while the OOB IIP$_3$ was +15 dBm at 6-MHz offset. The blocker 1-dB gain compression point ($B_{1dB,CP}$) is also improved. The S_{11} degrades to only −8 dB. It may be noted that while in-band IIP$_3$ and $B_{1dB,CP}$ improve (due to lower gain and higher reflected power), the OOB IIP$_3$ is lower. This is because the voltage swing across the RDAC
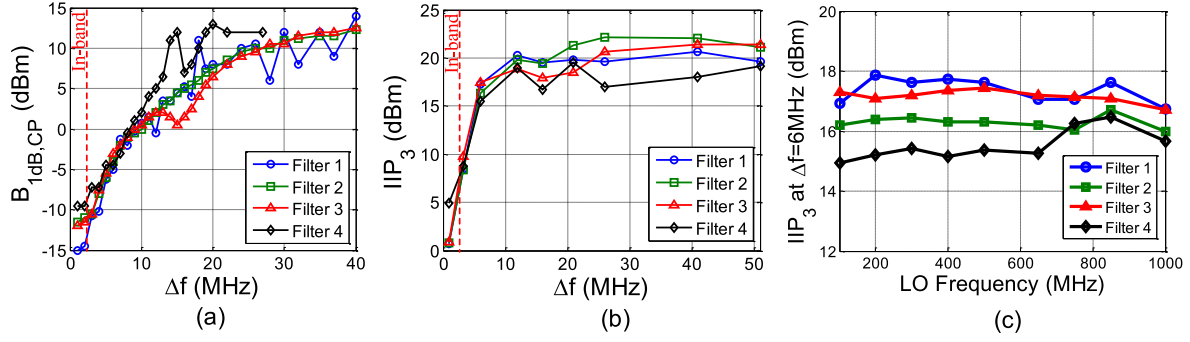
Fig. 24. Measured (a) $B_{1dB,CP}$ and (b) IIP_3 and for various frequency offsets from the center frequency for 5-MHz RF BW filters at $F_{lo} = 500$ MHz. (c) OOB IIP_3 at $\Delta f = 6$ MHz for LO varied from 0.1 to 1 GHz.
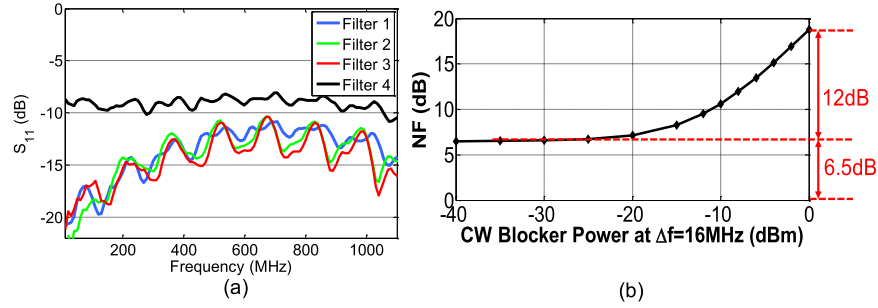

Fig. 25. (a) Measured S_{11} for filters designed with and without an S_{11} constraint. (b) Measured NF in the presence of a continuous-wave blocker at $\Delta f = 16$ MHz for a 5-MHz RF BW at $F_{lo} = 500$ MHz (for filter 1).

TABLE I

COMPARISON TABLE

Metric	[3] ISSCC '14	[7] ISSCC '13	[11] JSSC '12	[12] ISSCC '15	This Work	
					FA	FA with S_{11} constraint
Architecture	DT Analog	N-path	Noise cancelling mixer-first	Mixer-first with 2nd order baseband	FA	FA with S_{11} constraint
Technology	65nm	65nm	40nm	65nm	65nm	65nm
RF Frequency (GHz)	1.8-2.5	0.1-1.2	0.08-2.7	0.5-3	0.1-1	0.1-1
RF Input	Single-ended	Differential	Single-ended	Differential	Single-ended	Single-ended
BW* (MHz)	0.2-20	8	4	2-60	2.5-40	2.5-40
Stop-band Rejection (Transition BW)	>70dB (~4×BW)	59dB (12×BW)	NA	>30dB (~5×BW)	>48dB (3.5×BW)	>35#dB (2.5#×BW)
In-band IIP_3 (dBm)	-7	-12	-20	NA	+5	+1
Out-of-band IIP_3 (dBm)	NA	+26 (Δf=6.25×BW)	+13.5 (Δf=20×BW)	-4.8 (Δf=2×BW)	+15 (Δf=1.2×BW)	+17 (Δf=1.2×BW)
Out-of-band IIP_2 (dBm)	+85	NA	+55	NA	+55 (Δf=1.2×BW)	+60 (Δf=1.2×BW)
$B_{1dB,CP}$ (dBm)	NA	+7 (Δf=6.25×BW)	-2 (Δf=20×BW)	-10 (Δf=2×BW)	+2 (Δf=2×BW) +13 (Δf=4×BW)	+0.7 (Δf=2×BW) +8 (Δf=4×BW)
S_{11} (dB)	<-10	-5 to -8	<-8.8	<-10	<-8	<-10
Gain (dB)	82	25	72	50	15.4	18.9
NF (dB)	3.2-4.5	2.8	1.9	4.7	7-10	6-7.5
Supply Voltage (V)	1.2/2	1.2	1.2/2.5	1.2/2.5	1.2/1	1.2/1
Power Consumption	55-65mW	18-57.6mW 15-48mA	35.1-78mW 27-60mA	96mW	66.8-74+mW 56-62+mA	66.8-74+mW 56-62+mA
Area (mm²)	1.1	0.27	1.2	7.8	2	2

*RF bandwidth (twice the baseband bandwidth)

#For filter 1 (tunable by trading off transition bandwidth and stop-band rejection)

+Varies with F_{lo} (70mW/59mA for F_{lo} =0.5GHz)

(and its switches) is higher due to higher instantaneous (and average) resistance values for filter 4. The measured results for filters 2 and 3 (designed for matching, but with higher transition bands) are similar to filter 1, with linearity and S_{11} not differing significantly. The $B_{1dB,CP}$ does visibly degrade around the filter sidelobes in the transition band.
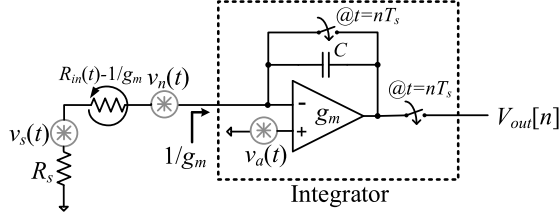
Fig. 26.   Equivalent circuit for noise analysis.

Table I compares this paper with recent designs. The filtering performance achieved is sharper than that of most prior art. Comparable linearity is attained, but for blockers at much lower frequency offsets than prior art, with good S_{11} and acceptable NF. Note that while overall gain is lower, this is because the other works include gain stages after the front-end filtering (to combine signals from multiple paths). Additional gain stages after the baseband are not expected to change NF or OOB linearity, especially since the baseband sampling rate is low.

VI. CONCLUSION

This paper introduced a programmable receiver front end based on a periodically time-varying baseband. Using an LPTV resistor, a sharp programmable analog-FIR filtering response was achieved at baseband. A four-path mixer was then used to upconvert the filter to RF to achieve sharp band-pass filtering. Further, it was shown that impedance matching to the antenna can be achieved by imposing an additional S_{11} constraint on the FIR filter design. The implemented receiver achieved high close-in linearity with > 17 dBm of IIP$_3$ at only $1.2 \times$ BW frequency offset while achieving a wideband impedance match, with S_{11} better than -10 dB throughout the measured LO range of 0.1–1 GHz.

APPENDIX A
NOISE FACTOR OF THE LPTV BASEBAND

The noise performance of the receiver's baseband equivalent circuit can be analyzed based on the circuit shown in Fig. 26. The op-amp is built as a simple g_m stage with input-referred noise voltage $v_a(t)$, while the noise sources corresponding to the source R_s and time-varying resistance $R_{in}(t) - 1/g_m$ are $v_s(t)$ and $v_n(t)$, respectively. Note that the input impedance of the op-amp, $1/g_m$, is separated from the controlled resistance variation $R_{in}(t)$ for simplifying the noise expressions. The noise sources are considered white Gaussian with autocorrelations

$$R_{ss}(t_1, t_2) = E[v_s(t_1)v_s(t_2)] = 2kTR_s\delta(t_1 - t_2)$$
$$R_{nn}(t_1, t_2) = E[v_n(t_1)v_n(t_2)] = 2kT[R_{in}(t_1) - g_m^{-1}]$$
$$\times \delta(t_1 - t_2)$$
$$R_{aa}(t_1, t_2) = E[v_a(t_1)v_a(t_2)] = 2kT\frac{\gamma}{g_m}\delta(t_1 - t_2) \quad (19)$$

where k is the Boltzmann's constant, T is the temperature in Kelvin, and $\delta(.)$ is the Dirac delta function. Using superposition, the output voltage due to the current integrated on the

capacitor can be obtained as

$$V_{out}[n] = \int_{t=(n-1)T_s}^{nT_s} \frac{v_s(t) + v_n(t) + v_a(t)}{C[R_s + R_{in}(t)]}dt. \quad (20)$$

From (20), the autocorrelation of the output voltage samples can be calculated to be $R_{oo}[m, n] = E[V_{out}[m]V_{out}[n]] =$

$$E\left[\frac{1}{C^2}\int_{t_1=(m-1)T_s}^{mT_s}\int_{t_2=(n-1)T_s}^{nT_s}\right.$$
$$\frac{v_s(t_1)v_s(t_2)}{[R_s + R_{in}(t_1)][R_s + R_{in}(t_2)]}dt_1 dt_2$$
$$+\frac{1}{C^2}\int_{t_1=(m-1)T_s}^{mT_s}\int_{t_2=(n-1)T_s}^{nT_s}$$
$$\frac{v_a(t_1)v_a(t_2)}{[R_s + R_{in}(t_1)][R_s + R_{in}(t_2)]}dt_1 dt_2$$
$$+\frac{1}{C^2}\int_{t_1=(m-1)T_s}^{mT_s}\int_{t_2=(n-1)T_s}^{nT_s}$$
$$\left.\frac{v_n(t_1)v_n(t_2)}{[R_s + R_{in}(t_1)][R_s + R_{in}(t_2)]}dt_1 dt_2\right]$$

with cross terms going to zero since the noise sources are independent. Moving the $E[.]$ operator into the integrals and evaluating using (19) gives $R_{oo}[m, n] =$

$$\frac{1}{C^2}\int_{t_1=(m-1)T_s}^{mT_s}\int_{t_2=(n-1)T_s}^{nT_s}$$
$$\frac{2kTR_s\delta(t_1 - t_2)}{[R_s + R_{in}(t_1)][R_s + R_{in}(t_2)]}dt_1 dt_2$$
$$+\frac{1}{C^2}\int_{t_1=(m-1)T_s}^{mT_s}\int_{t_2=(n-1)T_s}^{nT_s}$$
$$\frac{2kT\gamma g_m^{-1}\delta(t_1 - t_2)}{[R_s + R_{in}(t_1)][R_s + R_{in}(t_2)]}dt_1 dt_2$$
$$+\frac{1}{C^2}\int_{t_1=(m-1)T_s}^{mT_s}\int_{t_2=(n-1)T_s}^{nT_s}$$
$$\frac{2kT[R_{in}(t_1) - g_m^{-1}]\delta(t_1 - t_2)}{[R_s + R_{in}(t_1)][R_s + R_{in}(t_2)]}dt_1 dt_2.$$

Each double integral is nonzero only when $t_1 = t_2$, i.e., when $m = n$. Hence,

$$R_{oo}[n, n] = E[V_{out}^2[n]] = \frac{2kT}{C^2}\int_{t=(n-1)T_s}^{nT_s}\frac{R_s}{[R_s + R_{in}(t)]^2}dt$$
$$+\frac{2kT\gamma}{C^2}\int_{t=(n-1)T_s}^{nT_s}\frac{g_m^{-1}}{[R_s + R_{in}(t)]^2}dt$$
$$+\frac{2kT}{C^2}\int_{t=(n-1)T_s}^{nT_s}\frac{[R_{in}(t) - g_m^{-1}]}{[R_s + R_{in}(t)]^2}dt \quad (21)$$

and $R_{oo}[m, n] = 0$ for $m \neq n$. Note that since $R_{in}(t)$ is periodic with period T_s, $R_{oo}[n, n]$ is independent of n. Thus, the autocorrelation, $R_{oo}[m, n]$ is wide sense stationary and is given by

$$R_{oo}[m, n] = R_{oo}[m - n] = E[V_{out}^2[0]]\delta[m - n]. \quad (22)$$

Note that the autocorrelation is only a single-tap long. Hence, the output power spectral density (PSD) is white and is

given by

$$S_{oo}(e^{j\omega}) = \mathcal{F}\{R_{oo}[n]\} = \frac{2kT}{C^2} \int_{t=(n-1)T_s}^{nT_s} \frac{R_s}{[R_s + R_{in}(t)]^2} dt$$

$$+ \frac{2kT\gamma}{C^2} \int_{t=(n-1)T_s}^{nT_s} \frac{g_m^{-1}}{[R_s + R_{in}(t)]^2} dt$$

$$+ \frac{2kT}{C^2} \int_{t=(n-1)T_s}^{nT_s} \frac{[R_{in}(t) - g_m^{-1}]}{[R_s + R_{in}(t)]^2} dt \quad (23)$$

where the first, second, and final terms correspond to noise from R_s, the op-amp, and $R_{in}(t) - 1/g_m$, respectively. The relative noise contribution of each noise source with respect to R_s can be calculated by simply dividing the entire expression in (23) with the first term, thus giving the noise factor F

$$F = 1 + \frac{\gamma}{g_m R_s} + \frac{\text{mean}[(R_{in}(t) - g_m^{-1})/(R_s + R_{in}(t))^2]}{R_s \text{mean}[1/(R_s + R_{in}(t))^2]}. \quad (24)$$

APPENDIX B
NOISE CONTRIBUTION FROM ALIASING

The noise factor F captures the relative contributions of each noise source with respect to R_s. However, the output sampling implies that the NF due to the source R_s is not 0 dB due to aliasing, and so must be included separately. After aliasing, the noise power at baseband frequency of Δf is the sum of noise power at Δf and all its aliasing frequencies. Hence, given the sampling frequency $F_s(= 1/T_s)$ and the effective filter frequency response $G(f)$ [obtained in (6)], the output noise PSD due to R_s at frequency Δf is given by $2kTR_s \sum_{n=-\infty}^{\infty} |G(\Delta f + nF_s)|^2$, where k is the Boltzmann's constant and T is the temperature in Kelvin. The noise PSD due to R_s is simply the first term in (23), and so

$$2kTR_s \sum_{n=-\infty}^{\infty} |G(\Delta f + nF_s)|^2 = \frac{2kT}{C^2} \int_{t=0}^{T_s} \frac{R_s}{[R_s + R_{in}(t)]^2} dt. \quad (25)$$

Clearly, the PSD is white [as is the case for all noise sources as shown in (23)].

On the other hand, without aliasing, the noise PSD would have been $2kTR_s|G(\Delta f)|^2$ (the input noise density times the square of the gain of the filter). Thus, the noise degradation from aliasing at baseband frequency Δf is given by

$$F_{\text{aliasing}}(\Delta f) = \frac{2kTR_s \sum_{n=-\infty}^{\infty} |G(\Delta f + nF_s)|^2}{2kTR_s|G(\Delta f)|^2} \quad |\Delta f| \le \frac{F_s}{2}. \quad (26)$$

The dc gain of the filter is

$$G(\Delta f = 0) = \int_{t=0}^{T_s} \frac{dt}{C[R_s + R_{in}(t)]}$$

and so using (25) and (26), it can be shown that

$$F_{\text{aliasing}}(\Delta f = 0) = \frac{\text{mean}[(R_s + R_{in}(t))^{-2}]}{\{\text{mean}[(R_s + R_{in}(t))^{-1}]\}^2}. \quad (27)$$

Since the numerator in (26) is constant (due to the total noise PSD being white), (26) can be finally expressed as

$$F_{\text{aliasing}}(\Delta f) = \left| \frac{G(\Delta f = 0)}{G(\Delta f)} \right|^2 F_{\text{aliasing}}(\Delta f = 0)$$

$$= \left| \frac{G(\Delta f = 0)}{G(\Delta f)} \right|^2 \frac{\text{mean}[(R_s + R_{in}(t))^{-2}]}{\{\text{mean}[(R_s + R_{in}(t))^{-1}]\}^2}. \quad (28)$$

REFERENCES

[1] M. Nekovee, "Cognitive radio access to TV white spaces: Spectrum opportunities, commercial applications and remaining technology challenges," in *Proc. IEEE Symp. New Front. Dyn. Spectr.*, Apr. 2010, pp. 1–10.

[2] A. A. Abidi, "The path to the software-defined radio receiver," *IEEE J. Solid-State Circuits*, vol. 42, no. 5, pp. 954–966, May 2007.

[3] M. Tohidian, I. Madadi, and R. B. Staszewski, "A fully integrated highly reconfigurable discrete-time superheterodyne receiver," in *IEEE Int. Solid-State Circuits Conf. (ISSCC) Dig. Tech. Papers*, Feb. 2014, pp. 1–3.

[4] Y. Xu and P. R. Kinget, "A switched-capacitor RF front end with embedded programmable high-order filtering," *IEEE J. Solid-State Circuits*, vol. 51, no. 5, pp. 1154–1167, May 2016.

[5] A. El Oualkadi, M. El Kaamouchi, J.-M. Paillot, D. Vanhoenacker-Janvier, and D. Flandre, "Fully integrated high-Q switched capacitor bandpass filter with center frequency and bandwidth tuning," in *Proc. IEEE Symp. Radio Freq. Integr. Circuits (RFIC)*, Jun. 2007, pp. 681–684.

[6] A. Ghaffari, E. A. M. Klumperink, M. C. M. Soer, and B. Nauta, "Tunable high-Q N-path band-pass filters: Modeling and verification," *IEEE J. Solid-State Circuits*, vol. 46, no. 5, pp. 998–1010, May 2011.

[7] M. Darvishi, R. van der Zee, and B. Nauta, "A 0.1-to-1.2 GHz tunable 6 th-order *N*-path channel-select filter with 0.6 dB passband ripple and +7 dBm blocker tolerance," in *IEEE Int. Solid-State Circuits Conf. (ISSCC) Dig. Tech. Papers*, Feb. 2013, pp. 172–173.

[8] S. Hameed, M. Rachid, B. Daneshrad, and S. Pamarti, "Frequency-domain analysis of *N*-path filters using conversion matrices," *IEEE Trans. Circuits Syst. II, Exp. Briefs*, vol. 63, no. 1, pp. 74–78, Jan. 2016.

[9] C. Andrews and A. C. Molnar, "A passive mixer-first receiver with digitally controlled and widely tunable RF interface," *IEEE J. Solid-State Circuits*, vol. 45, no. 12, pp. 2696–2708, Dec. 2010.

[10] A. Mirzaei and H. Darabi "Analysis of imperfections on performance of 4-phase passive-mixer-based high-Q bandpass filters in SAW-less receivers," *IEEE Trans. Circuits Syst. I, Reg. Papers*, vol. 58, no. 5, pp. 879–892, May 2011.

[11] D. Murphy *et al.*, "A blocker-tolerant, noise-cancelling receiver suitable for wideband wireless applications," *IEEE J. Solid-State Circuits*, vol. 47, no. 12, pp. 2943–2963, Dec. 2012.

[12] R. Chen and H. Hashemi, "Reconfigurable SDR receiver with enhanced front-end frequency selectivity suitable for intra-band and inter-band carrier aggregation," in *IEEE Int. Solid-State Circuits Conf. (ISSCC) Dig. Tech. Papers*, Feb. 2015, pp. 1–3.

[13] S. Hameed, M. Rachid, B. Daneshrad, and S. Pamarti, "Frequency-domain analysis of a mixer-first receiver using conversion matrices," in *Proc. IEEE Int. Symp. Circuits Syst. (ISCAS)*, May 2015, pp. 541–544.

[14] M. Rachid, S. Pamarti, and B. Daneshrad, "Filtering by aliasing," *IEEE Trans. Signal Process.*, vol. 61, no. 9, pp. 2319–2327, May 2013.

[15] N. Sinha, M. Rachid, S. Pavan, and S. Pamarti, "Design and analysis of an 8 mW, 1 GHz span, passive spectrum scanner with > +31 dBm out-of-band IIP3 using periodically time-varying circuit components," *IEEE J. Solid-State Circuits*, vol. 52, no. 8, pp. 2009–2025, Aug. 2017.

[16] S. Hameed, N. Sinha, M. Rachid, and S. Pamarti, "A programmable receiver front-end achieving >17 dBm IIP3 at < 1.25× BW frequency offset," in *IEEE Int. Solid-State Circuits Conf. (ISSCC) Dig. Tech. Papers*, Jan./Feb. 2016, pp. 446–447.

[17] J. Kaiser and R. Schafer, "On the use of the I₀-sinh window for spectrum analysis," *IEEE Trans. Acoust., Speech, Signal Process.*, vol. ASSP-28, no. 1, pp. 105–107, Feb. 1980.

[18] T. Parks and J. McClellan, "Chebyshev approximation for nonrecursive digital filters with linear phase," *IEEE Trans. Circuit Theory*, vol. CT-19, no. 2, pp. 189–194, Mar. 1972.

[19] S.-P. Wu, S. Boyd, and L. Vandenberghe, "FIR filter design via spectral factorization and convex optimization," in *Applied and Computational Control, Signals, and Circuits*, vol. 1, B. Datta, Ed. Boston, MA, USA: Birkhäuser, 1999, ch. 5, pp. 215–245.

[20] L. R. Rabiner, "The design of finite impulse response digital filters using linear programming techniques," *Bell Syst. Tech. J.*, vol. 51, no. 6, pp. 1177–1198, Jul. 1972.

[21] S. Hameed and S. Pamarti, "A time-interleaved filtering-by-aliasing receiver front-end with >70 dB suppression at $< 4\times$ bandwidth frequency offset," in *IEEE Int. Solid-State Circuits Conf. (ISSCC) Dig. Tech. Papers*, Feb. 2017, pp. 418–419.

Sameed Hameed (S'13–M'17) received the B.Tech. degree in electrical engineering from IIT Madras, Chennai, India, in 2011, and the M.S. and Ph.D. degrees in electrical engineering from the University of California, Los Angeles (UCLA), CA, USA, in 2013 and 2017, respectively.

In 2013, he joined Broadcom, Irvine, CA, USA, as an RFIC Design Intern. From 2016 to 2017, he was an RFIC Design Intern at Silvus Technologies, Los Angeles, CA, USA, where he is currently an RFIC Engineer. His current research interests include the RF transceiver designs with an emphasis on signal processing techniques.

Dr. Hameed was a recipient of an Electrical Engineering Department Fellowship in 2013 for placing first in the 2013 Ph.D. preliminary exam in circuits and embedded systems, a UCLA Graduate Division Fellowship in 2014, the Broadcom UCLA Fellowship during the 2015–2016 academic year, the Dissertation Year Fellowship and the MediaTek UCLA Fellowship during the 2016–2017 academic year, the IEEE SSCS 2015–2016 Pre-Doctoral Achievement Award, the 2016–2017 SSCS Student Travel Grant, and the UCLA Electrical Engineering Department's 2016-2017 Distinguished Ph.D. Dissertation in Circuits and Embedded Systems Award.

Sudhakar Pamarti (S'98–M'03) received the B.Tech. degree in electronics and electrical communication engineering from IIT Kharagpur, Kharagpur, India, in 1995, and the M.S. and Ph.D. degrees in electrical engineering from the University of California, San Diego, CA, USA, in 1999 and 2003, respectively.

From 1995 to 1997, he was at Hughes Software Systems, New Delhi, India, and from 2003 to 2005, he was at Rambus Inc., Sunnyvale, CA, USA, developing embedded software and firmware for a wireless communication system, and high-speed I/O circuits, respectively. He is currently a Professor of electrical and computer engineering with the University of California, Los Angeles, CA, USA. His current research interests include the integrated circuit designs with special focus on developing algorithmic techniques to overcome circuit impairments.

Dr. Pamarti was a recipient of the National Science Foundation's CAREER Award. He has served as an Associate Editor for both the IEEE TRANSACTIONS ON CIRCUITS AND SYSTEMS I AND II. He currently serves on the Technical Program Committee of the IEEE Custom Integrated Circuits Conference and the IEEE International Solid-State Circuits Conference.